Structures 91 (2026) 112603

Contents lists available at ScienceDirect

Structures

journal homepage: www.elsevier.com/locate/structures

Flexural performance of prestressed geopolymer concrete beams: Experimental tests and numerical study

Guoxu Zhao [a], Gao Ma [a,b,*], Hyeon-Jong Hwang [c], Caijun Shi [a,**], Yunxing Du [a]

[a] College of Civil Engineering, Hunan University, Changsha 410082, China
[b] State Key Laboratory of Bridge Safety and Resilience, Hunan University, Changsha 410082, China
[c] Department of Architecture and Architectural Engineering, Seoul National University, 1 Gwanak-ro, Seoul 08826, Republic of Korea

ARTICLE INFO

Keywords:
Geopolymer concrete
Prestressed beams
Flexural behavior
T-beams
DIC

ABSTRACT

With the implementation of carbon neutrality goals, geopolymer concrete (GPC) has shown great potential for reducing carbon dioxide emissions in the industrial sector. However, current research on GPC structural elements remains limited, particularly with regard to the flexural behavior of prestressed GPC beams, which is still largely unexplored. In this study, an experimental investigation was carried out on a total of 14 prestressed T-beams containing 12 GPC specimens and 2 PCC control specimens to examine flexural behavior under different parameters including reinforcement ratio, prestressing tendons stress level, and cross-sectional configuration. The test results indicate that GPC beams generally exhibit lower flexural stiffness and cracking moments compared with conventional concrete beams, primarily due to the lower elastic modulus of GPC and crack resistance. Nevertheless, no significant difference was observed between the two materials in terms of ultimate compressive strength. The applicability of both Chinese code GB 50010–2010 and American code ACI 318–25 to predicting the flexural stiffness, cracking moment, and ultimate strength of the tested beams was evaluated. Moreover, this study adopts three-dimensional digital image correlation (DIC-3D) technology to measure and visualize the strain distribution over the flange surface of prestressed GPC beams. Finally, finite element analysis was conducted to simulate the performance of the prestressed GPC beams, with parametric studies performed to assess the effects of reinforcement ratio and prestressing ratio.

1. Introduction

Geopolymers are typically produced from pozzolanic or other aluminosilicate-rich materials, often incorporating industrial by-products and mineral wastes. Compared with the production of Portland cement concrete (PCC), replacing ordinary Portland cement with geopolymer binders can reduce carbon dioxide emissions by up to 75% [1,2]. Another key pathway for carbon reduction in geopolymer concrete (GPC) is its ability to make extensive use of construction and demolition waste. Studies have shown that recycling construction waste through geopolymerization yields more favorable outcomes than simply incorporating construction waste as a supplementary cementitious material in PCC [3].

In recent years, GPC structures have attracted growing attention as it integrates the mechanical advantages of environmental benefits of geopolymer materials [4,5]. To advance its practical application in engineering, it is essential to investigate the mechanical performance of GPC structures, with particular emphasis on the structural behavior of GPC beams. In terms of flexural performance of GPC beams, various studies have reported that GPC beams exhibit mechanical behavior similar to that of conventional reinforced concrete (RC) beams. Venkatachalam et al. [6], Monfardini et al. [7], Yost et al. [8], Prinsse et al. [9], and Lee et al. [10] investigated the influence of longitudinal reinforcement ratio on the flexural and shear behaviors of slag-based GPC beams, and concluded that their flexural and shear performance is comparable to that of ordinary concrete beams. Consequently, existing design codes for flexure and shear of conventional RC beams are applicable to GPC beams. Similarly, Prachasaree [11] evaluated the strength parameter effects of fly ash-based GPC beams under flexural, shear, and torsional loading using experimental data and several design

* Corresponding author at: College of Civil Engineering, Hunan University, Changsha 410082, China.
** Corresponding author.
E-mail addresses: zhaoguooxu@hnu.edu.cn (G. Zhao), magao@hnu.edu.cn (G. Ma), hwanghj@snu.ac.kr (H.-J. Hwang), cshi@hnu.edu.cn (C. Shi), duyunxing@hnu.edu.cn (Y. Du).

https://doi.org/10.1016/j.istruc.2026.112603
Received 28 March 2026; Received in revised form 12 June 2026; Accepted 7 July 2026
Available online 16 July 2026

codes (such as ACI 318–25 [12], AS3600 [13], CSA [14], and CIB-FIP [15]), and reported that the predictions achieved acceptable accuracy. On the other hand, some studies have revealed different findings. Alex [16] conducted a comparative investigation on the flexural behavior of fly ash-based GPC beams and conventional concrete beams, showing that the average cracking load of GPC beams was about 22% higher, with larger deflection as well as improved load-carrying capacity and ductility. Similarly, Ahmed [17] studied nine fly ash-based GPC beams reinforced with carbon fiber reinforced polymer (CFRP) bars and three PCC beams, and found that the flexural performance of GPC beams significantly improved with increasing reinforcement ratio. Compared with PCC beams, GPC beams exhibited narrower crack widths, while ACI 440.1R−15 [18] underestimated their flexural strength.

With ongoing advancements in concrete production technologies, prestressed concrete has emerged as an economically efficient solution for long-span structures. The potential of GPC in prestressed applications has been investigated, demonstrating that its mechanical performance is comparable to that of conventional ordinary PCC with the same grade [17]. In particular, understanding the behavior of prestressed GPC beams is critical for facilitating the broader adoption of prestressed GPC in factory-based segmental precast construction. Despite this, limited experimental studies on prestressed GPC beams are available. Kobayashi et al. [19] performed flexural tests of prestressed rectangular GPC beams using alkali-aggregate reaction concrete, and reported that the load-deflection relationship was similar to that of conventional concrete, despite a moderate reduction of the peak load. Sonal et al. [20] proposed a mix design for GPC and tested four concrete beams, only two of which were prestressed geopolymer beams subjected to flexural test. The study demonstrated that prestressed GPC beams exhibited greater load-carrying capacity compared with their non-prestressed counterparts of the same batch. Magnuson [21,22] investigated geopolymer mix designs and concrete performance, and tested two prestressed GPC beams to evaluate flexural and shear behaviors. Theoretical predictions of ACI 318–19 [23] agreed well with the test results. Neupane and Hadigheh [24] examined the mechanical properties of GPC with a compressive strength of 50 MPa cured at ambient temperature. The indirect tensile and flexural strengths of GPC were approximately 27% higher than those of the counterpart PCC concrete. Muthuramalingam et al. [25] developed a mix design for prestressed concrete utility poles using low-calcium fly ash activated with sodium-based solutions, and observed the reduced deformation in the prestressed poles compared to PCC poles. Kastiukas et al. [26] studied the effect of curing methods (i.e., conventional oven curing and microwave radiation) on the compressive strength of GPC, and reported that microwave radiation reduced curing time for prestressed concrete to achieve the target strength. In contrast to these studies, Qian and Zhang [27] investigated the flexural behavior of GPC beams and reported that the initial stiffness decreased, cracking load decreased, and crack widths increased. The stiffness degradation was attributed to a lower elastic modulus and the presence of structural cracking. In addition, both the Chinese [28] and American codes [29] specify the effective flange width of composite beams in the elastic stage, and they adopt the same values for the plastic stage, which is inherently conservative [30]. Whether these provisions remain valid for geopolymer concrete requires further investigation. With the aid of current DIC−3D technology, obtaining the strain distribution across the flange of T-beams would provide a more reliable basis for analyzing the effective flange width.

In summary, available experimental studies on prestressed GPC members are limited, and the existing researches do not comprehensively address all influencing factors, such as concrete strength, reinforcement ratio, cross section configuration, and prestressing ratio. Moreover, finite element models lack experimental validation for prestressed GPC beams. As a result, there remains a notable gap in systematic investigations and well-established design theories for prestressed GPC beams. Given this context, it is necessary to conduct a comprehensive study on their structural behavior and to develop a complete mechanical performance evaluation framework, providing both theoretical guidance and empirical data for future research and engineering applications. For this reason, the present study investigated the structural performance of prestressed GPC beams using a mix design based on fly ash and finely ground blast furnace slag as raw materials, activated with a sodium-based solution. The GPC was cured under ambient conditions to facilitate precasting in the factory. Ordinary PCC of the same grade (50 and 70 MPa) was used as a control, and the flexural performance of both prestressed PCC and GPC beams was compared. Current design code application and numerical analysis results were also verified.

2. Materials and test methods

2.1. Raw materials

GPC generally features diverse mix proportions, and variations in mix constituents inevitably lead to distinct mechanical properties [31]. The raw materials adopted to prepare GPC in the present experiment fall into three categories: powders, alkali activators, and aggregates. The powders used in this study include slag and fly ash. The addition of slag to concrete increases its drying shrinkage, whereas the incorporation of fly ash reduces this shrinkage [32]. When fly ash is added to GPC, it extends the setting time but lowers the compressive strength [33]. Further, the use of NaOH in the activator increased concrete strength, while proper mixing of Na_2CO_3 resulted in reasonable setting time, workability, and compressive strength. The slag has a density of 2880 kg/m^3 and a specific surface area of 426 m^2/kg, while the fly ash has a density of 2310 kg/m^3 and a fineness of 257 m^2/kg. The average particle size of slag is 18.10 μm with a median diameter (d_{50}) of 13.9 μm, whereas the fly ash is classified as Class F, with an average particle size of 37.03 μm and d_{50} of 24.04 μm. The alkali activator consists of NaOH, sodium silicate (water glass), and sodium carbonate. The activator solution was prepared one day prior to casting, sealed, and stored at room temperature to prevent carbonation and moisture loss.

Coarse aggregate consisted of crushed stones with particle size ranging from 5 mm to 20 mm and a density of 1623 kg/m^3 . Fine aggregate was river sand with the maximum particle size of 4.51 mm and a density of 1466 kg/m^3 . The mix proportions of GPC significantly affect its performance [34], and the specific mix proportions used in this study are presented in Table 1. P.O42.5 R cement was used for C50 strength grade, and P.O52.5 R cement was used for C70 strength grade. The mix proportions of ordinary PCC used in this study are listed in Table 2.

2.2. Specimens

Fig. 1 shows the beam specimen configuration. To ensure flexural failure without shear failure, shear span-to-depth ratio was set to 4.3. D8 stirrups with a spacing of 100 mm were provided in accordance with GB 50010–2010 [28]. To minimize cracking at the beam top surface caused by concrete shrinkage and prestress-induced camber, additional D6 bars were arranged at the top of the beams. Further, sufficient anchorage length was provided at both ends of the constant moment zone to prevent tendon slip during loading. According to GB 50010–2010 [28], the required anchorage lengths for 15.2 mm prestressing tendons in C50 and C70 concrete are 1900 mm and 1596 mm, respectively. In this study, the distance from the loading point to each beam end was set at 2000 mm, which satisfied the anchorage length requirement. The control prestressed beam had a height of 300 mm, a web width of 170 mm, and a flange width of 340 mm, reinforced with two prestressing tendons of 15.2 mm diameter (Fig. 1**(a)**). Two additional 20 mm diameter deformed bars were placed at the beam bottom (Fig. 1**(b)**), to investigate the effect of reinforcement ratio. To investigate the influence of flange width and thickness on the flexural performance of GPC beams, flange width of (340, 510, and 850 mm) and flange thickness of (60 and

Table 1
Mix proportion of GPC.

(kg/m^3)	Slag	Fly ash	Sand	Gravel	Na_2CO_3	Sodium silicate solution	NaOH	Water
GPC50	350	116	674	1055	12	163.2	12.3	83.3
GPC70	397	100	661	1034	17	214.2	15.2	38.8

Table 2
Mix proportion of PCC.

(kg/m^3)	Cement	Slag	Fly ash	Silica fume	Sand	Gravel	Superplasticizer	Water
PCC50	457	-	114	-	696	1044	4.57	160
PCC70	450	120	-	20	610	1070	15	138

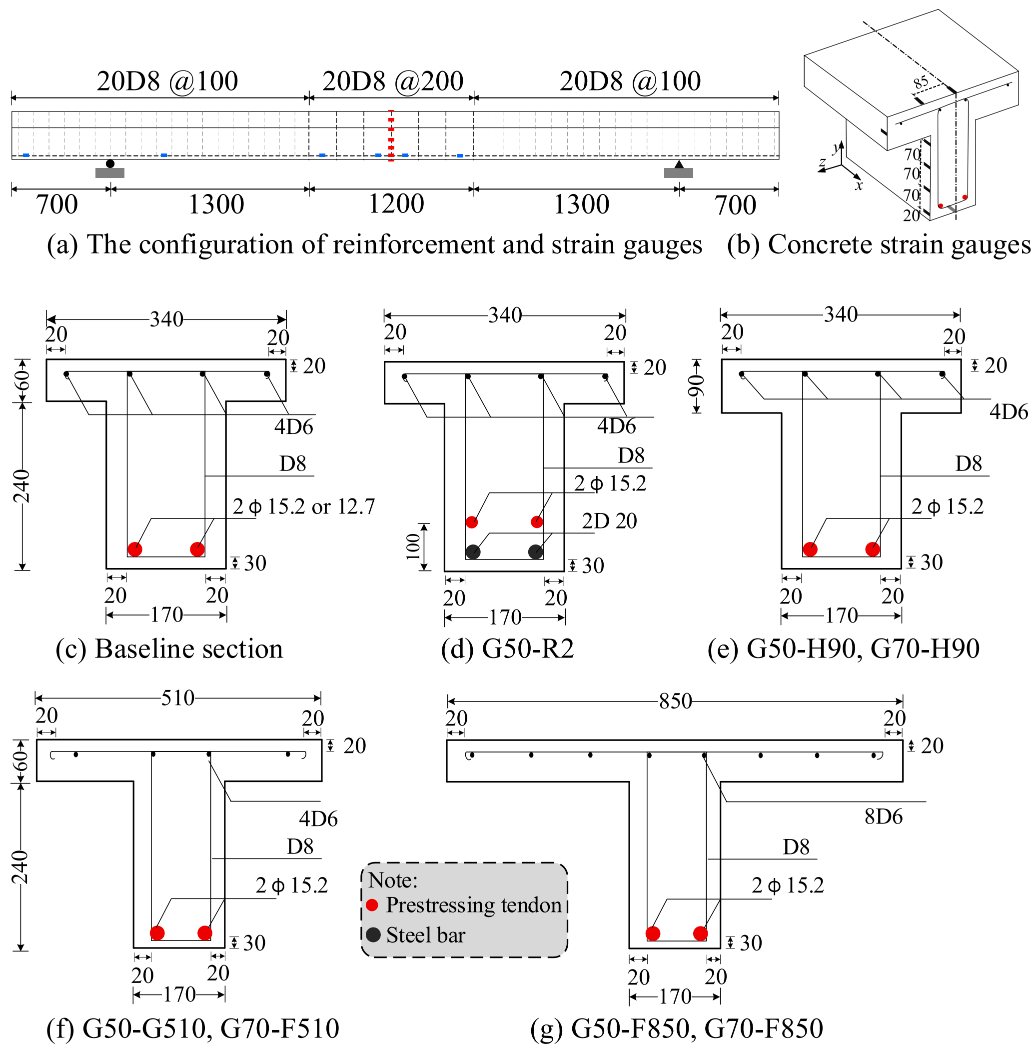

Fig. 1. Geometry and reinforcement details of prestressed beams (unit: mm).

90 mm) were considered. The main test parameters were concrete strength, reinforcement ratio, and prestressing ratio. All specimens were designed based on the reference section shown in Fig. 1**(a)**, with 15.2 mm prestressing tendons as the default. Specimens were labeled according to concrete type and test parameters: C and G denoted ordinary PCC and GPC, respectively, while R, D, P, F and H represented reinforcement ratio, tendon diameter, prestressing ratio, flange width and thickness, respectively. For example, the specimen labeled G70-F850 refers to a GPC beam with a compressive strength of 70 MPa and a flange width of 850 mm. The specimen matrix and detailed parameters are summarized in Table 3.

Prestressing tendons were tensioned on a couple of prestressing beds to the designed control stress (Fig. 2**(a)**). The tendon stresses measured by force sensors after anchorage (excluding prestress losses due to concrete compression) are summarized in Table 3. Following tendon anchorage, reinforcement assembly, formwork installation, and concrete casting were carried out (Fig. 2**(b)**). The concrete casting procedure followed the method described in the literature [35]. The properties of reinforcements and tendons can be seen in Table 4.

According to GB/T 50081–2019 [36], the compressive strength f_{cu} of concrete was measured using 150 mm × 150 mm × 150 mm standard cubes. The axial compressive strength ($f_c = \alpha_{c1} f_{co}$) and the axial tensile

Table 3
Details of specimens.

No.	Specimens	f_{co} (MPa)	h_f (mm)	b_f (mm)	Longitudinal reinforcement	f_{ps0} (MPa)	Prestressing ratio (%)
1	C50	56.40	60	340	2TD15.2	1230.57	66.16
2	C70	70.47	60	340	2TD15.2	1189.07	63.93
3	G50	50.78	60	340	2TD15.2	1230.57	66.16
4	G50-R2	50.15	60	340	2TD15.2 + 2RD20	1189.07	63.93
5	G50-D12.7	39.23	60	340	2TD12.7	1189.07	63.93
6	G50-F510	53.83	60	510	2TD15.2	1201.57	64.60
7	G50-F850	50.00	60	850	2TD15.2	1134.64	61.00
8	G50-H90	45.66	90	340	2TD15.2	1189.07	63.93
9	G70	63.37	60	340	2TD15.2	1230.57	66.16
10	G70-P50%	65.82	60	340	2TD15.2	1143.07	51.46
11	G70-D12.7	60.60	60	340	2TD12.7	1109.49	59.65
12	G70-F510	65.20	60	510	2TD15.2	1201.57	64.60
13	G70-F850	64.42	60	850	2TD15.2	1134.64	61.00
14	G70-H90	65.88	90	340	2TD15.2	1143.07	61.46

Note: f_{co} is the concrete compressive strength tested from cube, h_f and b_f are the thickness and width of flange, respectively. In the description of longitudinal reinforcement, "T" represents tendons and "R" represents rebars. f_{ps0} is the effective prestress stress obtained from load sensor before tendon release.

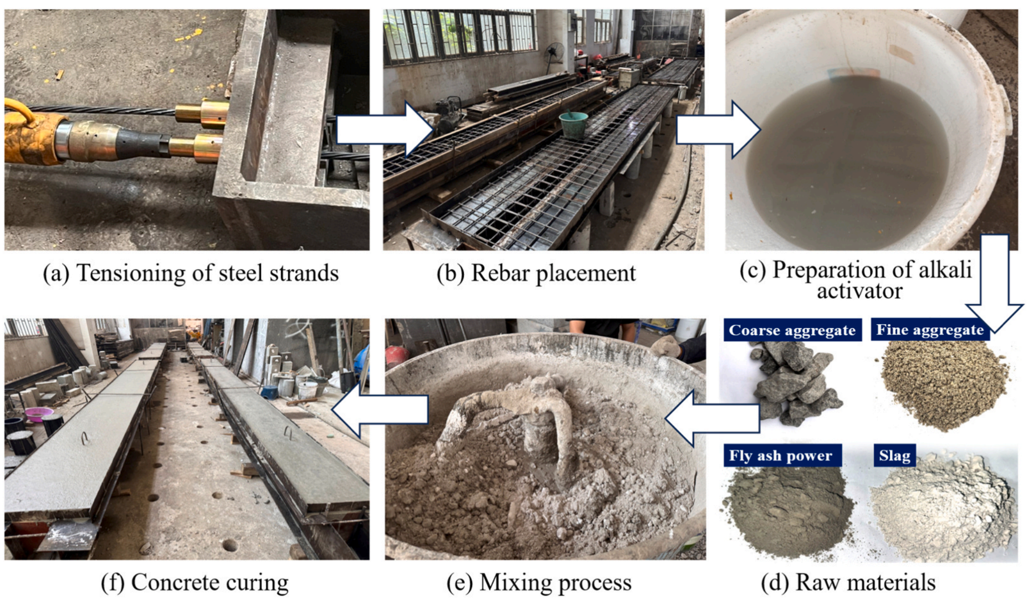

Fig. 2. Manufacturing process of specimens.

Table 4
Mechanical properties of steel bars and tendons.

Steel bars and tendons	Diameter (mm)	f_y (MPa)	f_u (MPa)
HRB400	8	398.4	546.2
HRB400	6	399.5	554.1
Strand−12.7	12.7	1860.2	1910.3
Strand−15.2	15.2	1860.5	1922.7

strength (f_t=0.395(f_{co})$^{0.55}$) were calculated in accordance with GB/T 50152–2012 [37], where α_{c1} is 0.76 and 0.79 for concrete with strengths of 50 MPa and 70 MPa, respectively. The elastic modulus of the 50 MPa and 70 MPa PCC was 32.39 GPa and 34.71 GPa, respectively, whereas the corresponding value for geopolymer concrete was 24.19 GPa and 28.62 GPa.

During concrete preparation, slag, fly ash, and sand were first added and mixed for 3 min to achieve uniformity. The alkali activator was then added and mixed for 2 min, followed by the coarse aggregate, which was mixed for an additional 5 min until a homogeneous mixture was obtained (Fig. 2**(e)**). For each batch, at least three 150 × 150 × 150 mm cubes were prepared to determine compressive strength. After casting, the beam surface was covered with a plastic film to prevent moisture loss, and water spraying was applied daily during early curing to enhance surface humidity and reduce cracking due to shrinkage. All specimens were cured at room temperature until the testing date. Once the concrete had reached at least 75% of its design compressive strength, the tendons were released. A gradual stress-release method was adopted, in which the prestressing force was reduced to below 10% of the tendon yield strength (f_{py}) using threaded clamps before cutting, thereby avoiding sudden fracture of the tendons and ensuring sufficient anchorage length at the beam ends.

2.3. Experimental program

Four-point loading was applied to the prestressed GPC beams. The constant bending region was 1200 mm, and the span length was 3800 mm. The experimental setup is shown in Fig. 3. A total of five displacement gauges were installed on the beam, to measure the deflection at the mid-span and loading points and the possible slip of the prestressing tendons at both ends. Strain gauges were attached on the tendon at the mid-span, loading point, quarter-span location, and beam end. Force-controlled loading was applied using a 100-ton hydraulic

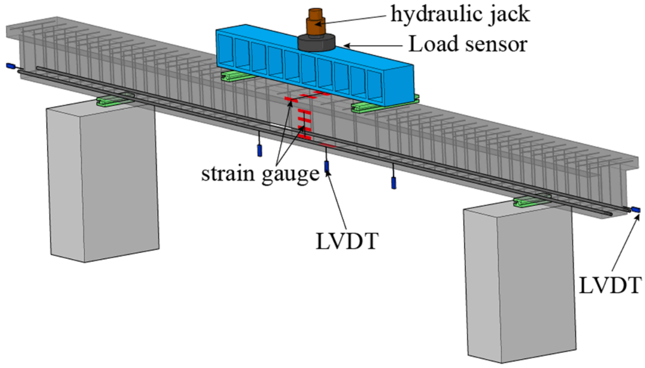

Fig. 3. Test setup.

jack at 10 kN step before cracking and 20 kN step after cracking. A 100-ton load sensor was placed on the top of the hydraulic jack to measure the applied load. The deflection, load at the first crack, and crack propagation were recorded during each increment.

As shown in Fig. 4, digital image correlation (DIC) technique was employed to capture vertical surface images of the beam specimen in order to track speckle patterns. In addition, a DIC−3D system was installed on the beam top surface to obtain strain distributions across the wide flange and evaluate the shear lag effect. To verify the accuracy of the DIC−3D deformation measurements, strain gauges were attached to the top surface of the flange on the side where the DIC−3D measurement was conducted.

3. Test results

3.1. Load-deflection relationship

Although the reinforcement ratios of all specimens satisfied the minimum reinforcement requirements (0.15%) specified in GB 50010–2010 [28], the overall reinforcement ratio were relatively low. As a result, the majority of specimens exhibited a failure mode governed by prestressing tendons yielding (Fig. 5). Only five beams experienced crushing of the top concrete in the compression zone. Fig. 5 shows that flexural behavior of prestressed GPC beams is comparable to that of prestressed PCC beams. From the load-deflection curves, it can be observed that the most notable difference between the GPC and PCC beams lies in the significantly higher initial stiffness exhibited by the PCC beams, while the difference in the peak load is relatively small. A more detailed discussion is provided in the subsequent sections.

The typical load-deflection curve of the beams can be divided into four distinct stages, as shown in Fig. 6. Three critical points can be identified: the first cracking load (point A); the point where the number of cracks ceased to increase (point B); and the yielding of reinforcement (point C). Accordingly, the flexural behavior may be classified into the following four stages. (1) Elastic stage (OA): At the initial loading stage, mid-span deflection and measured strains increased linearly with applied load, showing elastic flexural behavior. (2) Crack development stage (AB): Once the load exceeded the cracking load, cracks first appeared at mid-span and then propagated toward the supports. The spacing of cracks was approximately equal to the stirrup spacing. With further loading, flexure-shear cracks formed beneath the loading points. The number of cracks stabilized, and no new cracks developed. (3) Stabilized cracking stage (BC): The number of cracks remained essentially constant, but crack widths and heights increased progressively. Occasional “snapping” sounds were heard from the prestressing tendons, as cracks developed, and the slip of steel tendon occurred. As cracks widened, the restraining effect of reinforcement diminished, and the prestressing tendons approached yielding. (4) Yielding stage (CD): When the load reached 80–90% of the peak load, mid-span deflection continued to increase while the load plateaued, indicating yielding of the prestressing tendons. The main crack rapidly extended toward the bottom of the T-beam flange, the neutral axis shifted upward, and failure occurred due to crushing of the top flange.

The flexural stiffness of all specimens is summarized in Table 5. Compared with PCC beams made of C50 and C70 concrete, the initial flexural stiffness of GPC beams decreased by approximately 30.0% and 38.8%, respectively. This reduction can be explained by the lower elastic modulus of GPC relative to ordinary concrete for beams of identical cross-section. With the increase in the flange dimensions, the moment of inertia of the beam cross-section increased, which naturally resulted in a significant improvement in the initial flexural stiffness of the specimens. After the load exceeded the elastic stage, the stiffness decreased significantly, and owing to the earlier cracking in the geopolymer concrete, this stiffness degradation was more pronounced in the GPC beams than in the PCC beams after cracking.

When the service load was considered approximately 50–70% of the load-carrying capacity, the average effective flexural stiffness of GPC beams made with C50 and C70 concrete decreased by 68.0% and 56.92%, respectively, compared to their PCC counterparts under service conditions. Unlike the initial stiffness, the flexural stiffness of GPC beams (G50-R2) with ordinary tensile reinforcement in the tension zone decreased more gradually. This is because the presence of the conventional reinforcement limited crack propagation, preventing significant stiffness degradation. In GPC beam specimens, compared to the constant moment zone, flexural cracks developed more slowly in reinforced areas; however, once cracking occurred, the stress in the prestressing tendons rapidly increased until yielding.

Table 6 compares the cracking moment and ultimate moment for each beam specimen. In general, the cracking moment of GPC beams are lower than those of PCC beams, primarily because the greater shrinkage

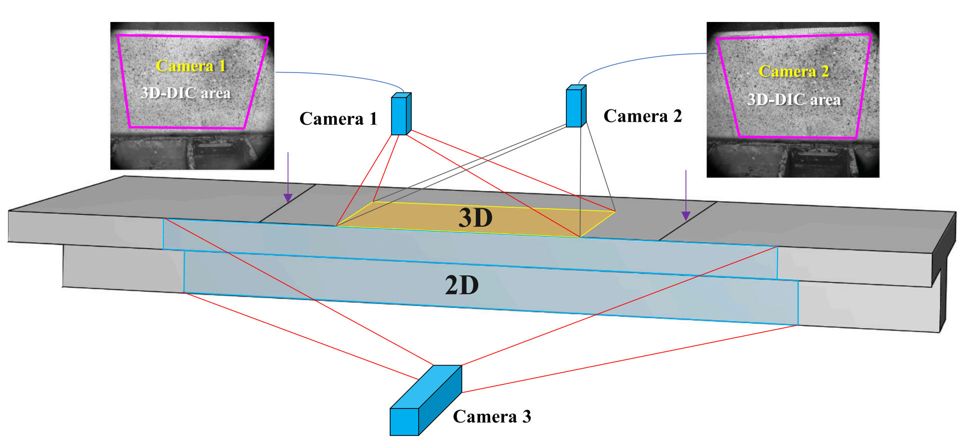

Fig. 4. DIC set up.

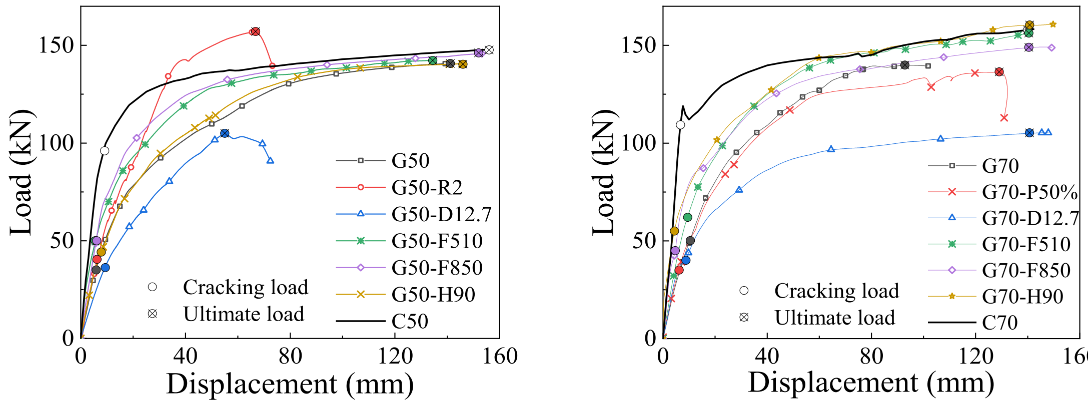

(a) 50 MPa grade concrete beams　　(b) 70 MPa grade concrete beams

Fig. 5. Load-deflection relationships of T-beam specimens.

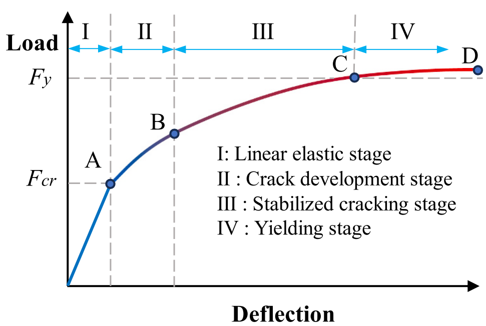

Fig. 6. Typical load-deflection curve of GPC beams.

and creep of GPC led to the formation of more microcracks [38,39]. Specifically, compared to PCC beams, the cracking moments of GPC beams decreased by 63.5% and 54.2% for C50 and C70 concretes, respectively, while the ultimate moments have almost no difference.

In all tests, the average sectional strain in the constant bending region generally conformed to the plane section assumption throughout the loading process. The strain of the mid-span section of the representative GPC beams is shown in Fig. 7. Thus, the full flexural response may be analyzed based on deformation compatibility.

3.2. Failure modes

During concrete curing, pronounced surface cracking was observed in GPC beams, which would be attributed to the camber induced by prestressing and the intrinsic drying shrinkage of the concrete. In contrast, ordinary concrete beams exhibited few or no cracks under the same conditions. Fig. 8 illustrates the crack patterns at failure and strain distributions measured by DIC for both PCC and GPC beams. Flexural cracks were initiated in the region of the maximum moment, followed by additional flexural cracks at the shear span region occurred as the load increased. With further loading, most of the flexural cracks propagated vertically, and subsequently inclined flexure-shear cracks developed. In the present study, cracks in GPC beams were uniformly distributed, with an average spacing of approximately 200 mm that corresponded closely to the stirrup spacing. Similar uniform crack distributions were reported by Ehsani et al. [40] and Faza et al. [41] for FRP-reinforced concrete beams. The crack development tendency forming at stirrup locations would be attributed to local bond deterioration between reinforcement and GPC, where the presence of stirrups introduces mechanical interlocking discontinuities and reduces friction resistance of stirrups, thus leading to stress concentrations in the surrounding concrete.

As shown in Fig. 8**(a)** and **(b)**, the maximum crack length of GPC beams was comparable to that observed in the PCC beams, indicating that the beams exhibited a similar compression zone depth at the peak load. For GPC specimens, increasing the reinforcement ratio led to a larger number of flexural cracks, a reduction in the average spacing between flexural cracks, and a decrease in maximum crack length (i.e.,

Table 5
Flexural stiffness of specimens.

No.	Specimens	$B_{s\text{-cr}}$ ($\times10^{12}$ N·mm^2)			$\frac{B_{s-exp}}{B_{s-GB}}$	$\frac{B_{s-exp}}{B_{s-ACI}}$	$B_{s-0.5}$ ($\times10^{12}$ N·mm^2)			$\frac{B_{s-exp}}{B_{s-GB}}$	$\frac{B_{s-exp}}{B_{s-ACI}}$
		$B_{s\text{-exp}}$	$B_{s\text{-GB}}$	$B_{s\text{-ACI}}$			$B_{s\text{-exp}}$	$B_{s\text{-GB}}$	$B_{s\text{-ACI}}$		
1	C50	18.51	16.63	17.09	1.11	1.08	14.32	4.82	15.94	2.97	0.90
2	C70	20.38	18.98	20.23	1.07	1.01	16.93	5.45	18.29	3.11	0.93
3	G50	12.94	12.23	12.57	1.06	1.03	4.58	4.71	6.22	0.97	0.74
4	G50-R2	14.06	12.17	12.51	1.16	1.12	4.52	4.13	5.58	1.10	0.81
5	G50-D12.7	7.90	11.80	12.49	0.67	0.63	2.96	4.72	7.06	0.63	0.42
6	G50-F510	12.11	14.20	14.74	0.85	0.82	5.27	4.66	6.63	1.13	0.79
7	G50-F850	18.07	17.34	17.78	1.04	1.02	6.99	4.61	7.59	1.51	0.92
8	G50-H90	10.00	12.04	12.59	0.83	0.79	3.72	4.29	5.68	0.87	0.65
9	G70	12.48	12.88	13.72	0.97	0.91	7.31	5.50	6.84	1.33	1.07
10	G70-P50%	9.90	12.31	13.12	0.80	0.75	5.67	6.76	7.44	0.84	0.76
11	G70-D12.7	7.11	12.48	13.48	0.57	0.53	5.72	5.34	7.21	1.07	0.79
12	G70-F510	18.07	15.26	16.38	1.18	1.10	6.96	4.95	6.97	1.41	1.00
13	G70-F850	17.83	18.41	19.66	0.97	0.91	5.00	5.16	8.24	0.97	0.61
14	G70-H90	18.16	11.68	12.12	1.55	1.50	5.85	3.60	4.81	1.62	1.22

Note: $B_{s\text{-cr}}$ and $B_{s-0.5}$ are flexural stiffness at cracking load and $0.5M_u$, respectively; $B_{s\text{-exp}}$ is the flexural stiffness obtained from experiment; $B_{s\text{-GB}}$ and $B_{s\text{-ACI}}$ are theoretical stiffness calculated by GB 50010–2010 and ACI 318–25, respectively.

Table 6
Cracking and ultimate moments of specimens.

No.	Specimens	$M_{cr\text{-}exp}$	$M_{cr\text{-}GB}$	$M_{cr\text{-}ACI}$	$\frac{M_{cr-exp}}{M_{cr-GB}}$	$\frac{M_{cr-exp}}{M_{cr-ACI}}$	$M_{u\text{-}exp}$	$M_{u\text{-}GB}$	$M_{u\text{-}ACI}$	$\frac{M_{u-exp}}{M_{u-GB}}$	$\frac{M_{u-exp}}{M_{u-ACI}}$
1	C50	62.40	24.47	24.40	2.55	2.56	95.36	133.71	96.19	0.71	0.99
2	C70	71.05	28.56	26.25	2.49	2.71	102.64	135.75	109.49	0.76	0.94
3	G50	22.75	24.62	24.49	0.92	0.93	91.46	133.81	96.81	0.68	0.94
4	G50-R2	26.26	24.05	24.01	1.09	1.09	102.12	136.22	96.31	0.75	1.06
5	G50-D12.7	23.53	20.24	20.64	1.16	1.14	69.62	96.33	76.08	0.72	0.92
6	G50-F510	32.50	21.94	22.43	1.48	1.45	92.50	135.84	97.09	0.68	0.95
7	G50-F850	32.50	19.51	20.45	1.67	1.59	93.70	137.69	93.10	0.68	1.01
8	G50-H90	28.73	22.25	22.53	1.29	1.28	91.20	133.10	92.35	0.69	0.99
9	G70	32.57	27.67	25.95	1.18	1.26	90.97	135.30	106.50	0.67	0.85
10	G70-P50%	22.75	19.19	18.71	1.19	1.22	88.71	134.73	102.78	0.66	0.86
11	G70-D12.7	26.00	22.37	21.23	1.16	1.22	68.40	96.71	80.24	0.71	0.85
12	G70-F510	40.30	25.71	24.31	1.57	1.66	101.61	136.97	108.22	0.74	0.94
13	G70-F850	29.25	22.21	21.94	1.32	1.33	96.84	137.81	102.11	0.70	0.95
14	G70-H90	35.75	27.14	24.55	1.32	1.46	104.28	135.43	107.38	0.77	0.97

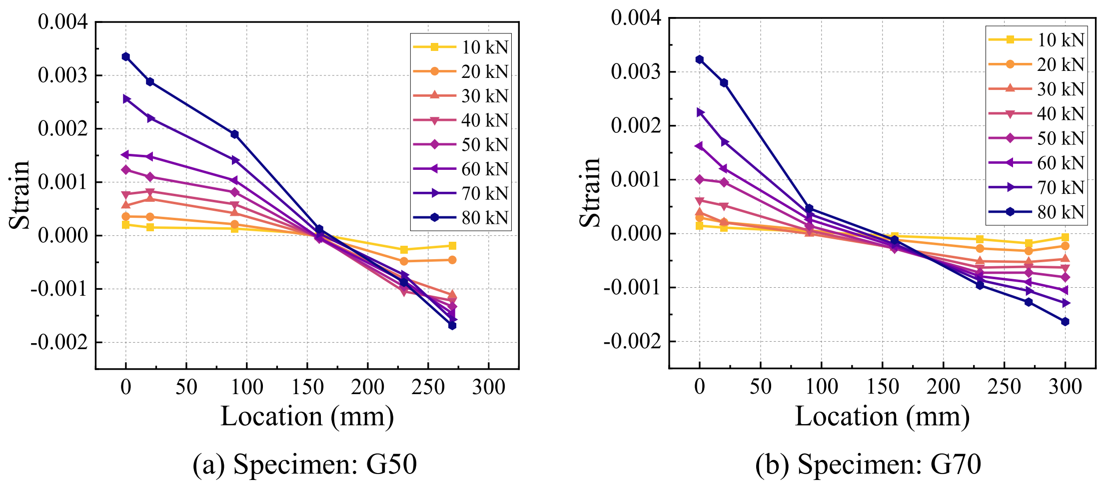

Fig. 7. Strain distribution in mid-span section of partial GPC beams.

an increase in the compression zone depth). However, the flange width and prestressing ratio did not influence the crack distribution. As shown in Fig. 8**(a)**, the cracking patterns of the GPC beams were similar to those of the PCC beams. At the final loading stage, a small number of cracks extended into the crushing zone of the GPC beams. Further, all beams developed extensive flexural cracking prior to the interaction between diagonal and flexural cracks, ensuring flexural failure rather than shear failure. At the peak load, bond-slip of prestressing tendons at the beam ends did not exceed 2.5 mm, indicating that no bond failure [42].

3.3. Effect of concrete strength and prestressing ratio

Fig. 9 compares the flexural stiffness and moment capacities between PCC and GPC beam specimens. As shown in Fig. 9**(a)** and **(b)**, PCC beams exhibited higher flexural stiffness than GPC beams with the same concrete strength. The initial stiffness of C70 PCC beam was higher than that of C50 PCC beam, which is consistent with the increase in elastic modulus with strength. However, the increase in initial stiffness for the GPC beams was not as evident, because GPC had a relatively low elastic modulus and its initial stiffness was influenced by multiple factors, resulting in greater variability. In contrast, the flexural stiffness under service conditions increased with the concrete strength. Cracking and ultimate moments for PCC and GPC beam specimens are compared in Fig. 9**(c)**. As the concrete strength increased from 50 MPa to 70 MPa, both PCC and GPC beams exhibited higher cracking moments corresponding to the increased compressive strength. Moreover, PCC beams demonstrated superior cracking moment compared to prestressed GPC beams, which is similar with observations reported in the existing study [43]. This discrepancy may be attributed to the use of steam curing in the literature [20], which likely reduced the development of microcracks during the curing process. As the concrete strength increased, the cracking moment also increased, which was attributed to the increase of the tensile strength of concrete. The ultimate moment was governed primarily by the compression zone depth, and the influence of concrete strength on the ultimate moment was minimal in this study. As seen in Table 5 and Table 6, a lower prestressing ratio reduced the initial stiffness, stiffness at service condition, and cracking moment of the beams, while having only a minor influence on the ultimate strength.

3.4. Effect of rebar ratio

Fig. 10 illustrates the influence of reinforcement ratio on the flexural stiffness and moment of GPC beam specimens. The flexural stiffness at initial and service conditions of the beams increased as the reinforcement ratio increased. For G50 concrete beams, the initial stiffness of specimens G50-R2 and G50 increased by 77.9% and 63.8% compared to specimen G50-D12.7, respectively, while for specimen G70, the corresponding increase was 57.9% compared to specimen G70-D12.7. As the reinforcement ratio increased, both the cracking and ultimate moments of the beams were significantly enhanced.

Increasing the reinforcement ratio proved to be the most effective method to improve the ultimate moment and flexural stiffness of under-reinforced GPC beams. Specifically, specimen G50 with 2A15.2 tendons exhibited the cracking moment of approximately 22.75kN·m and

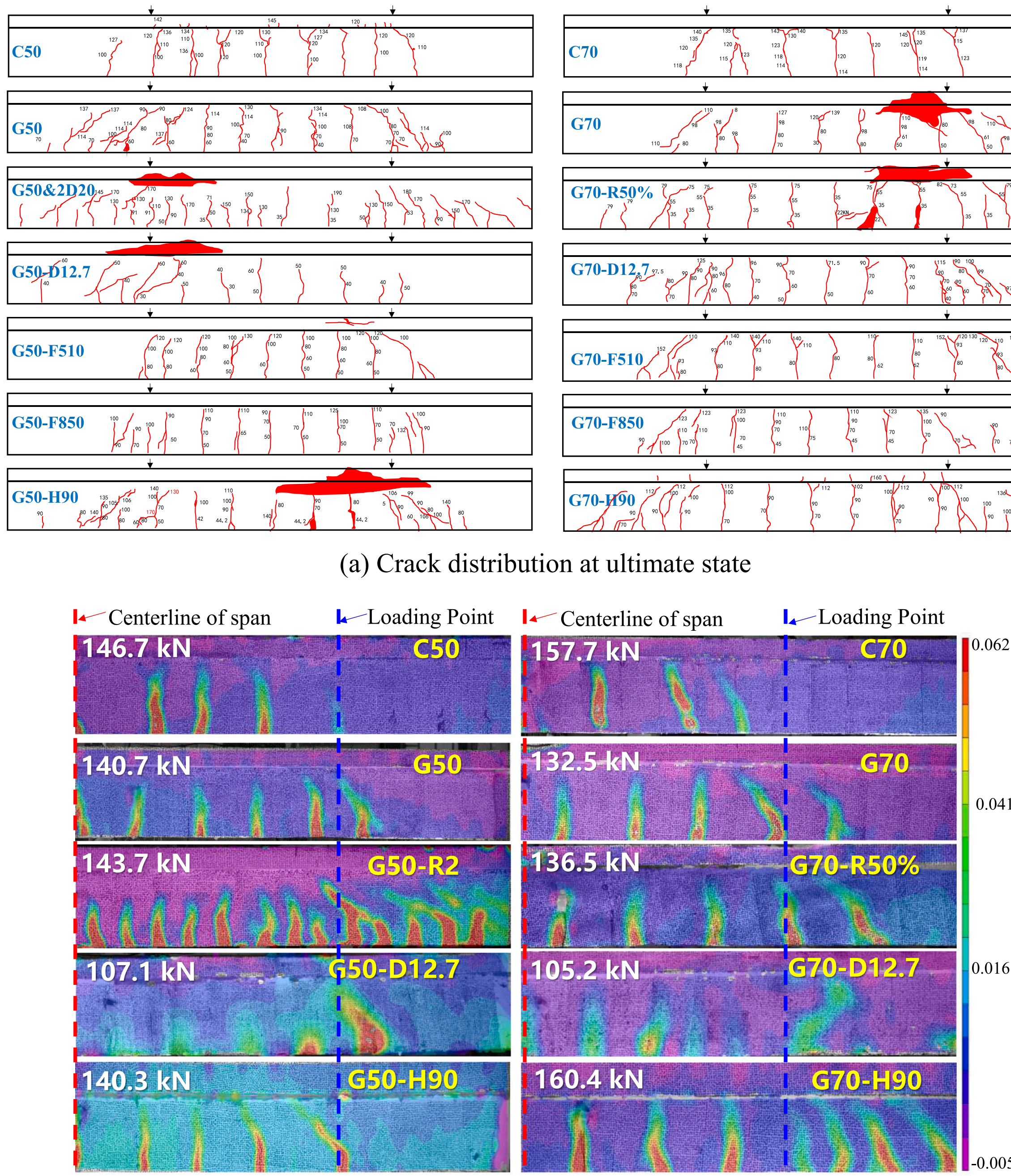

(b) DIC results at ultimate state

Fig. 8. Crack distribution and DIC results at ultimate state.

ultimate moment of 91.46 kN·m, maintaining its load-carrying capacity over the deflection of 80–140 mm, demonstrating good ductility and uniform crack distribution. In contrast, specimen G50-R2 with higher reinforcement ratio exhibited lower cracking load of 26.26 kN·m. After cracking, it retained considerable stiffness, resulting in significantly enhanced flexural stiffness but reduced ductility. On the other hand, specimen G50-D12.7 exhibited the lowest cracking load (23.53 kN·m) and ultimate load (69.62 kN·m).The reinforcement ratio has a noticeable influence on both the flexural stiffness and the flexural load-carrying capacity of the specimens.

3.5. Shear lag effect

To verify the validity of 3D digital image correlation (DIC−3D) techniques, both strain gauges and DIC−3D techniques were employed to comprehensively measure the strain distribution across the flange section of the T-beams. Fig. 11 compares the strains obtained from the two methods at different points. Due to the concentration of coarse aggregates and cracks, which may cause uneven strain distribution on the surface, the DIC strain data represent the average strain within 200 mm of the neutral axis. Note that strain gauge was malfunctioned in G70-F510. Overall, the strain trends measured by the strain gauges and DIC were consistent, increasing gradually with deflection, which validates the reliability of the DIC method even under large structural deformations. Besides, DIC measurements exhibited more continuous and smoother strain distributions in detail, whereas strain gauge data sometimes showed missing or fluctuating values at certain locations because the strain gauges measured only local deformation. The strain

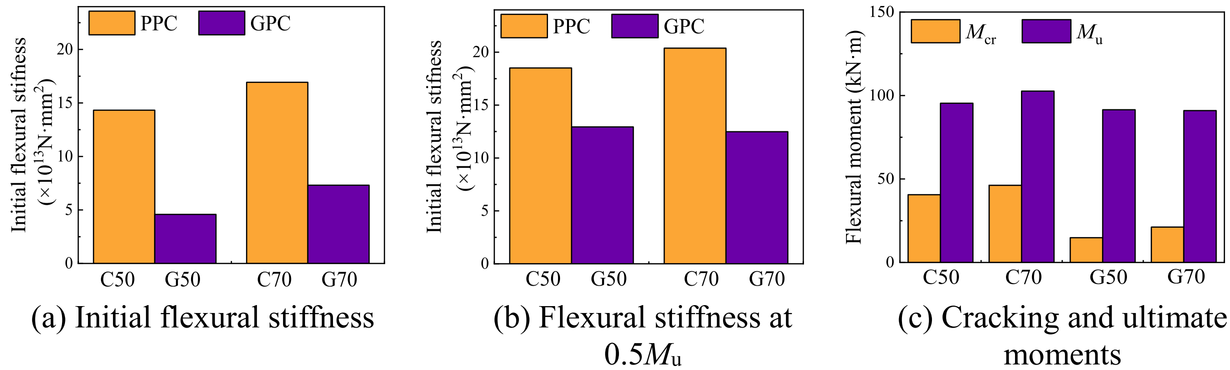

Fig. 9. Effect of compressive strength on the flexural behavior of GPC beams.

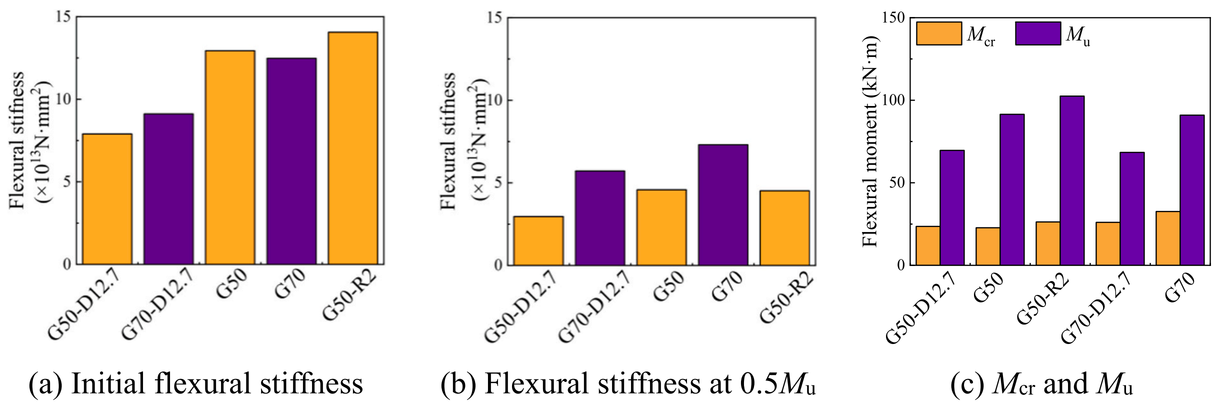

Fig. 10. Effect of rebar ratio on the flexural behavior of GPC beams.

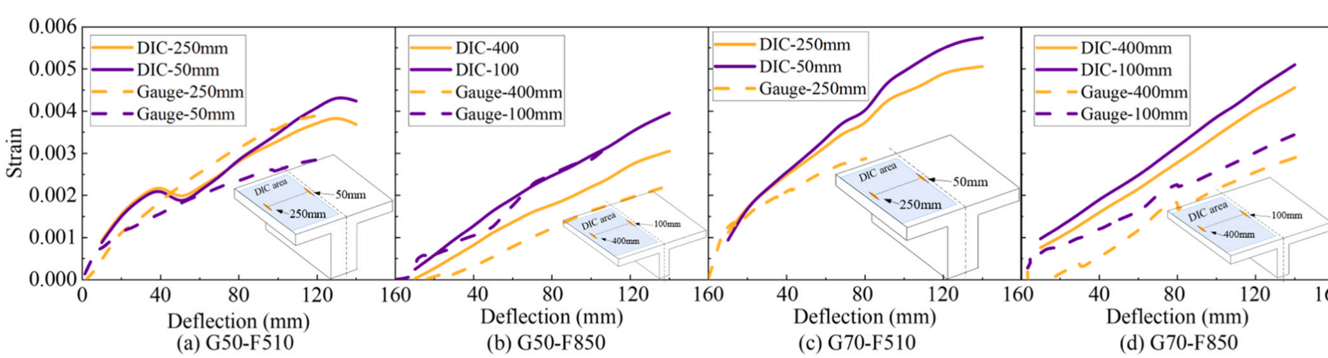

Fig. 11. Comparison of strain distribution between DIC and strain gauges.

distributions of G50-F850 and G70-F850 were not entirely consistent. This discrepancy can be attributed to the limited measurement range of strain gauges (approximately 100 mm) compared to the larger coverage of DIC. After concrete casting, prestressed GPC beams may develop cracks or microcracks at the top due to drying shrinkage and prestress-induced camber, which can lead to higher strain values during load period recorded by DIC.

Fig. 12 presents the full-section strain distribution obtained via DIC and the strain profiles along the width of the section. The DIC strain diagram shows the strain distribution within a range of approximately 400 mm around the mid-span, and the vertical direction includes data only within half of the flange width. During loading, the section strain distribution was highly non-uniform: strains were the largest near the central portion of the flange and gradually decreased toward the edges. The shear lag effect was more pronounced in the flange with a width of 850 mm (Fig. 12**(b)** and **(d)**), compared to the flange with a width of 510 mm (Fig. 12**(a)** and **(c)**). In addition, as the deflection increased, the shear lag effect became more pronounced. The dark blue regions in Fig. 12 correspond to initial shrinkage crack, which was first close, resulting in evident strain concentrations. This non-uniformity is primarily caused by the crack development and the heterogeneous deformation between coarse aggregates and mortar. Meanwhile, in specimen G50-F850, it can be observed that cracks also affect the strain values, with a sudden change appearing at about 200 mm along the width direction. Such full-field strain visualization, which is difficult to obtain using conventional strain gauges, provides critical insights into the deformation mechanisms of T-beams under flexural behavior.

In analyzing the DIC data, strains in the cracked regions were treated as visual indicators of crack evolution, while effective data were extracted from the continuous regions for the investigation of shear lag effects. This approach ensures the rationality of shear lag analysis while preserving information on the influence of cracks on the overall

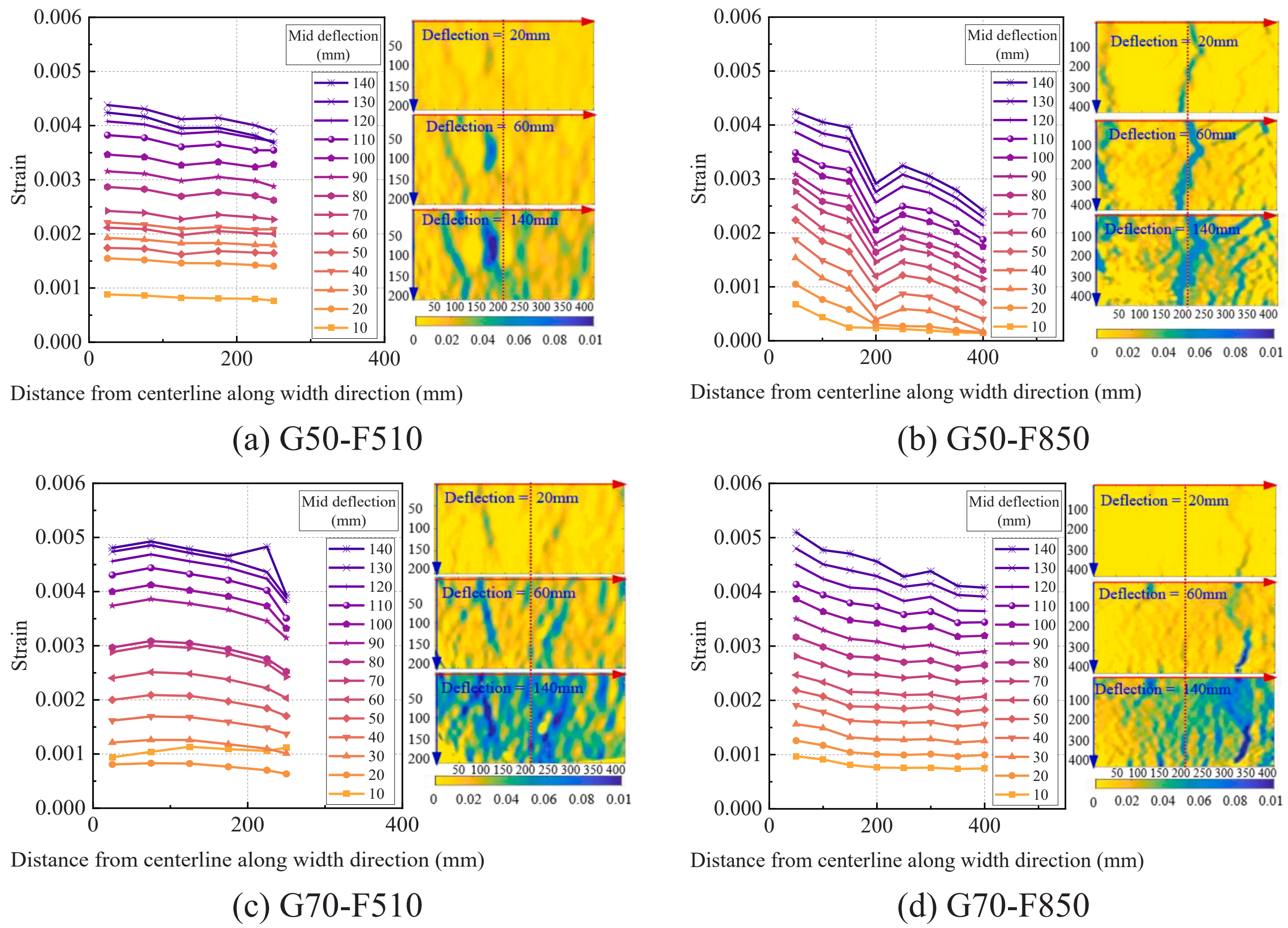

Fig. 12. Strain distributions measured by DIC (Note: In each image, the upper red axis represents the longitudinal direction, the blue arrow indicates the distance from centerline on width direction, and the red dot marks the midline along the longitudinal direction.).

structural response. Although the presence of cracks inevitably introduces additional uncertainty into the DIC measurements, it simultaneously provides valuable insights into structural damage, offering a basis for understanding the degradation of beam performance under realistic loading conditions.

3.6. Discussion

3.6.1. Cracking moment and flexural stiffness

It should be emphasized that the comparative analysis on cracking moment and flexural stiffness between prestressed GPC and PCC beams in this study is constrained by the limited experimental conditions and fixed GPC mix proportions adopted in the test. Universal conclusions regarding inherent performance differences between GPC and ordinary PCC cannot be generalized from the present test data alone. The discrepancy of the structural performance between GPC and PCC is significantly affected by the elastic modulus and tensile strength. For this reason, an analysis is conducted to determine whether the methods for calculating the stiffness and cracking moment of prestressed concrete beams, as specified in the GB 50010–2010 and ACI 318–25 [12,28], are applicable to GPC beams. The cracking moment specified in GB 50010–2010 [28] is as follows:

$$M_{cr} = (\sigma_{pc} + \gamma f_t)W_0 \tag{1}$$

where σ_{pc} is the concrete pre-compressive stress generated at the edge of the crack boundary by the pre-applied force, after all prestressing loss is deducted;f_t is the tensile strength of concrete; γ is the factor of inertia moment of cross-section, which can be taken as 1.5; and W_0 is the elastic resistance moment at the tension edge of the member's equivalent section.

The cracking moment of the prestressed beam specified in ACI 318–25 [12] is as follows:

$$M_{cr} = \frac{(f_r + \sigma_{pc})I_g}{y_t} \tag{2}$$

$$f_r = 0.62\lambda\sqrt{f_c'} \tag{3}$$

$$f_c' = 0.8 f_{co} \tag{4}$$

where I_g represents the inertia moment of the concrete gross section; y_t denotes the distance from the centroidal axis of the gross section (neglecting reinforcement) to the tension face; f_r is the modulus of rupture of concrete; f_c' is the standard cylindrical compressive strength; λ is the correction factor for concrete performance based on density, taken as 1.0 in this study; f_{cu} is the standard cubic compressive strength.

The cracking moment of prestressed GPC beams calculated from Eqs. (1) and (2) is summarized in Table 6. ACI 318–25 [12] (Eq. (2)) (with the range of 0.93 ~ 1.66) and GB 50010–2010 [28] (Eq. (1)) (with the range of 0.92 ~ 1.67) provided similar prediction results. The estimations of GPC beams in both codes are conservative. Besides, for ordinary concrete specimens in this experiment, the cracking moment was significantly underestimated.

GB 50010–2010 [28] specifies the effective stiffness of reinforced concrete flexural members as follows:

$$B_s = \frac{0.85E_cI_0}{\kappa_{cr} + (1-\kappa_{cr})\omega} \quad (5)$$

$$\omega = \left(1.0 + \frac{0.21}{\alpha_E\rho}\right)\left(1 + 0.45\gamma_f\right) - 0.7 \quad (6)$$

$$\gamma_f = \frac{(b_f - b)h_f}{bh_0} \quad (7)$$

where $\kappa_{cr} = \frac{M_{cr}}{M_k}$; E_c is the elastic modulus of concrete; I_0 is the moment of inertia of the cross-section after converting rebars area to concrete area; α_E is the ratio of the elastic modulus of steel to that of concrete; ρ is the tensile reinforcement ratio; b_f and h_f are the width and thickness of flange, respectively; h_0 is the effective height of the beam; and b is the width of web.

ACI 318–25 [12] uses the theory of the effective moment of inertia (Eq. (8)), to calculate the stiffness of prestressed concrete beams. The equivalent moment of inertia I_e is calculated from the concrete gross section inertia I_g and transformed cracked section inertia I_{cr}, which is then used to determine the stiffness of the component. The formula is relatively simple and easy to understand; however, the prediction accuracy is significantly influenced by the cracking moment M_{cr}.

$$B_s = E_cI_e \quad (8)$$

$$I_e = \left(\frac{M_{cr}}{M}\right)^3 I_g + \left[1 - \left(\frac{M_{cr}}{M}\right)^3\right] I_{cr} \quad (9)$$

.

Table 5 compares the predictions of flexural stiffness with the test results. The predictions of Eq. (5) align well with the experimental results. However, due to manufacturing errors in specimen G50-D12.7, the flexural stiffness was noticeably overestimated. The normalized mean and mean absolute error of the predicted stiffness at service for the GPC beams, based on GB 50010–2010 [28] and ACI 318–25 [12], are 1.12 and 0.2, and 0.82 and 0.176, respectively. Overall, GB 50010–2010 [28] is more suitable for predicting the short-term stiffness of GPC beams under flexural behavior. ACI 318–25 [12] predictions tend to be more unconservative and lower than the actual values. Thus, the GB 50010–2010 [28] for calculating the flexural stiffness is applicable to GPC beams.

3.6.2. Ultimate moment

In GB 50010–2010 [5], the bending moment of prestressed beams can be calculated as follows:

$$M_u = f_cbx\left(h_0 - \frac{x}{2}\right) + f_c\left(b_f - b\right)h_f\left(h_0 - \frac{h_f}{2}\right) + f_y{'}A_s{'}\left(h_0 - a_s{'}\right) \quad (10)$$

where h_0 is the effective height of cross-section; x is the compressive zone depth; $f_y{'}$ and $A_s{'}$ are the yield strength and cross-sectional area of compressive reinforcement, respectively; and $a_s{'}$ is the distance from the resultant force point of the longitudinal reinforcement in the compression zone to the compressed edge of the section.

In ACI 318–25 [12], the nominal flexural strength is calculated using an equation similar to that in the Chinese code, with the primary difference being the term representing the contribution of the prestressing tendons. The flexural strength is defined as follows:

$$M_u = A_{ps}f_{ps}\left(d_p - \frac{a}{2}\right) + A_sf_y\left(d - \frac{a}{2}\right) - A_s{'}f_y{'}\left(d' - \frac{a}{2}\right) \quad (11)$$

$$a = \frac{A_{ps}f_{ps} + A_sf_y - A'_sf'_y}{0.85f'_cb} \quad (12)$$

$$f_{ps} = f_{pu}\left\{1 - \frac{\gamma_p}{\beta_1}\left[\rho_p\frac{f_{pu}}{f'_c} + \frac{d}{d_p}\frac{f_y}{f'_c}\left(\rho - \rho'\right)\right]\right\} \quad (13)$$

where a is the depth of the equivalent rectangular concrete stress block; A_{ps} is the cross-sectional area of prestressing tendons; f_{ps} and f_{pu} is the stress in the prestressing tendons at the nominal flexural strength and nominal yield strength, respectively; γ_p is a factor for the type of prestressing tendon; β_1 is a factor related to the depth of an equivalent rectangular compressive stress block to the neutral axis depth; ρ_p is the prestressing tendon ratio ($= A_p/bd_p$); d_p and d_s are the effective depths of the prestressing tendons and mild tensile reinforcement, respectively; ρ and ρ' are the mild tensile and compressive reinforcement ratio, respectively.

As seen in Table 6, the mean value and coefficient of variation for flexural capacity predictions using GB 50010–2010 [28] are 0.71 and 0.035, respectively, while those obtained from ACI 318–25 [12] are 0.944 and 0.061. Eq. (11) predicted well the nominal flexural moment, with average ratio of test results to predictions ranging from 0.86 to 1.06. Thus, the ACI 318–25 [12] for calculating the ultimate moment is applicable to GPC beams, albeit with slightly unconservative predictions, which can be attributed to the absence of conventional longitudinal reinforcement in the test specimens. Compared with GB 50010–2010 [28], ACI 318–25 [12] provides a more accurate calculation of nominal flexural strength, primarily because it accounts for the prestressing steel stress at the ultimate limit state. In contrast, GB 50010–2010 [28] applies reduction factors to material strengths during design (e.g., the design value of 1860 MPa prestressing tendons is taken as 1320 MPa), which can also yield reasonably accurate results. GB 50010–2010 [28] is developed for flexural capacity calculation of balanced-reinforced beams. Deviations exist between predicted and actual strand stress when no reinforcing bars are arranged in the specimens. However, ACI 318–25 [12] remains somewhat conservative when evaluating T-shaped sections. Besides, Loov [44] reported that the prediction accuracy of ACI 318 was dependent on the amount and placement of the non-prestressed reinforcement.

3.6.3. Shear lag effect

Due to the lower elastic modulus of GPC compared with PCC, the shear strains in the concrete flange may prevent the cross-section from remaining plane, resulting in a non-uniform normal stress distribution along the slab width, called "shear lag" effect. Whether this phenomenon differs from that observed in ordinary concrete also requires further investigation. In terms of loading conditions and boundary conditions related to the cross-section configuration, the type of constraint can significantly influence the shear lag effect. Typically, the shear lag effect has a considerable impact on the calculation of the effective flange width of T-beams (refer to Fig. 13). To further investigate the mechanism of shear lag transfer and the shear lag effect in engineering practice, the effective flange width (b_{eff}) of specimens G50-F510, G50-F850, G70-F510 and G70-F850 is calculated as follows:

$$b_{eff} = \frac{\int_0^b \sigma(x, y)dx}{\sigma_{max}} \quad (14)$$

where σ is the measured stress accounting for shear deformations; and

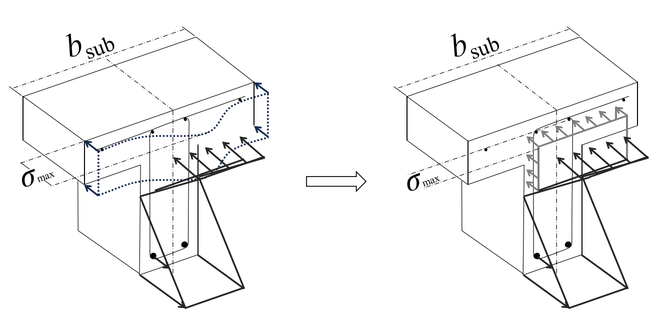

Fig. 13. Shear lag effect on beam moment.

σ_{max} is the maximum stress along the cross section.

The design approach specified in GB50010–2010 [28] adopts the allowable stress method. Its provisions for determining the effective flange width of composite beams are similar to those in ACI 318–25 [12]. The effective flange width is defined as the minimum of: (1) one-third of the span; (2) the spacing between the centerlines of two adjacent T-beams; and (3) twelve times the thickness of the RC slab outside the deck haunch. In the AASHTO [29], the effective flange width is taken as the minimum of: (1) one-quarter of the span; (2) $12h_f$ plus the larger of the web width or half the width of the top flange; and (3) the average spacing between adjacent T-beams. The comparison of the effective flange width b_{eff} and the flange width b_{sub} under different width-to-span ratios is shown in Fig. 14**(a)**. Given the relatively small width-to-span ratio in this study, both the GB50010–2010 [28] and AASHTO [29] indicate that the b_{eff} /b_{sub} should be taken as almost 1 (0.966 for AASHTO).

The effective flange width obtained from the full-section strain data extracted from DIC is shown in Fig. 14**(b)**. The effective width of the section increased as the deflection increased. The maximum effective flange width ratio of b_{eff} /b_{sub} at the ultimate moment in specimens G50-F510, G50-F850, G70-F510, and G70-F850 was 0.924, 0.767, 0.956, and 0.818, respectively. As the section size increased, the shear lag effect became more pronounced, resulting in a lower effective flange width. Additionally, for the same flange width, G70 concrete achieved a larger effective flange width ratio, compared to G50 concrete.

When the flange width was 510 mm, the effective flange widths specified in both GB50010–2010 [28] and AASHTO [29] were essentially identical to the flange width. In this study, however, the effective flange width measured in GPC slabs with a flange width of 850 mm was approximately 15% smaller than the code-specified values. Thus, directly applying the existing code provisions to GPC may not be sufficiently conservative.

4. Numerical analysis

4.1. Finite element model

To complement the experimental results, a three-dimensional finite element (FE) analysis of the prestressed GPC beams under direct loading was conducted using Abaqus. Concrete was modeled using C3D8R solid elements, with the concrete damage plasticity model adopted as the constitutive model, and the tensile constitutive behavior of PCC was defined according to GB 50010–2010 [28] (Eq. (15)), and GPC model was used according to the literature [45] (Fig. 15**(a)**). In addition, the plastic damage parameters of GPC are set identical to those of ordinary concrete as suggested by Hassan et al. [46]. Specifically, the dilation angle (φ), plastic potential eccentricity (e), initial biaxial-to-uniaxial compressive strength ratio (f_{b0}/f_{c0}), loading surface shape parameter (K_c), and viscosity parameter are specified as 37°, 0.1, 1.16, 2/3, and 0.005, respectively.

$$\sigma_c = f_{cm}\frac{\varepsilon_c}{\varepsilon_{cm}}\frac{n}{n-1+(\varepsilon_c/\varepsilon_{cm})^{nk}} \tag{15}$$

where f_{cm} is the concrete compressive peak stress; ε_{cm} is the strain corresponding to the peak stress; and $n = 0.8 + (f_{cm}/17)$. The value of k can be calculated as follows:

$$k = \begin{cases} 0.67 + (f_{cm}/62), & \varepsilon_c/\varepsilon_{cm} > 1 \\ 1, & \varepsilon_c/\varepsilon_{cm} \le 1 \end{cases} \tag{16}$$

.

Reinforcing bars and prestressing tendons were represented by T3D2 truss elements. Specifically, the transverse bars were embedded within the concrete, and the interaction between the transverse bars and concrete was modeled using an embedded bond approach, which has been shown to have negligible impact on the overall structural response [47, 48]. In this method, the reinforcement bars were considered axial members embedded in the solid concrete, ensuring that their displacement was consistent with the surrounding concrete. The bond behavior between prestressing tendons and concrete differs from that of ordinary reinforcement, gradually degrading with increasing interfacial shear stress. Thus, modeling the interaction requires specific assumptions, taking into account the bond-slip relationship between the tendons and concrete. In the FE model, prestressing tendons were connected to the concrete via nonlinear spring elements, with the bond-slip effect represented by the springs. The bond-slip relationship is described as follows (Fig. 15**(c)**):

$$\tau_{max} = 39.6{f'_c}^{0.25} - 76.5 \tag{17}$$

where τ_{max} is the maximum bond stress; τ_f in Fig. 15**(c)** is the residual friction stress, taken as $0.4\tau_{max}$; and δ_1 and δ_{max} are the bond-slip, taken as 3 mm and 12 mm, respectively.

Prestressing force was applied using the internal cooling method, and the relationship between stress and temperature is defined as follows:

$$\sigma = \alpha \Delta T E \tag{18}$$

where α is the length reduction factor per unit temperature (= 0.0186/(℃·MPa)); ΔT is the cooling temperature; and E_s is the elastic modulus of the prestressing tension (= 20 GPa). Note that the prestressing loss of

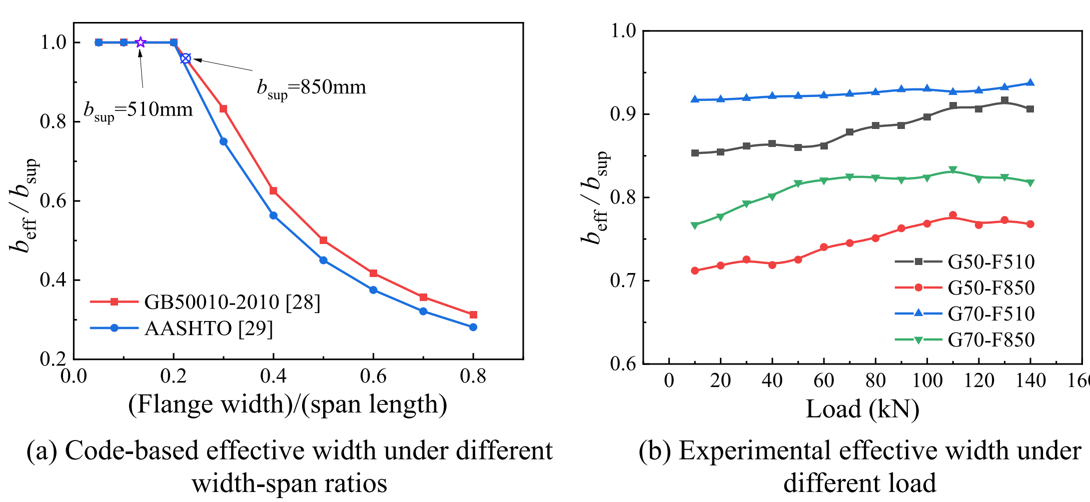

Fig. 14. Effective flange width comparison.

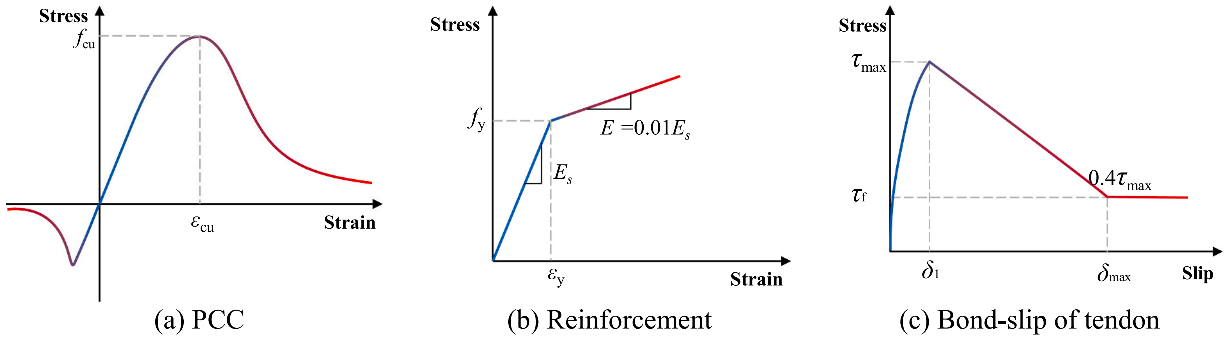

Fig. 15. Constitutive model used in FE model.

shrinkage and creep is not considered in this study.

Regarding mesh discretization, the mesh size along the beam length is set to 20 mm for the constant bending moment region at midspan, and 40 mm for the remaining regions.

4.2. Validation of FEA models

To validate the accuracy of the finite element model, the load-deflection curves obtained from the simulations of specimens C50 and G50-R2 were compared with the experimental results (Fig. 5), as well as with the crack development patterns (Fig. 8). The simulated load-deflection curves exhibited a similar trend to the experimental ones, and the discrepancies between the two remained within an acceptable range (Fig. 16**(a)**). Besides, the time-dependent prestress loss induced by concrete shrinkage and creep is not introduced into the current numerical model, which may also bring minor deviations between simulated and measured mechanical responses. However, the FE model did not account for the bond-slip effect between the stirrups or top reinforcement and the surrounding concrete, nor did it incorporate possible manufacturing defects or gaps. These simplifications may have led to a slight overestimation of the initial stiffness. Meanwhile, the crack pattern in Fig. 16**(b)** is similar to that in Fig. 8. This confirms that the FE model can effectively capture the mechanical behavior of both ordinary concrete and GPC beams.

4.3. Parametric study of GPC beams: effect of reinforcement ratio and prestressing ratio

Fig. 17**(a)** illustrates the effect of reinforcement ratio on the prestressed GPC beams. The specimen labels indicate the full reinforcement configuration of each beam. The three beams analyzed in the FEA correspond to reinforcement ratios of 1.8%, 2.5%, and 2.8%, respectively. As the reinforcement ratio increased, the load-carrying capacity improved, but its deformation capacity decreased. The maximum loads for reinforcement ratios of 1.8%, 2.5%, and 2.8% were 170.8 kN, 189.5 kN, and 199.7 kN, respectively, which represent increases of approximately 21.32%, 35.18% and 42.43% compared to specimen G50. The FEM analysis results indicate that increasing the bottom tensile reinforcement can enhance the load-carrying capacity, but for adequately reinforced beams, the improvement is less pronounced, as the load-carrying capacity is limited by the crushing of the top compressed concrete.

Analyses were also conducted for PGC beams with different prestressing ratio (Fig. 17**(b)**). All beams were designed with the same reinforcement ratio as specimen G50 (i.e., two 15.2 mm prestressing tendons), and only the prestressing ratio was varied in the parametric study. Prestressing ratio has a limited influence on the load-carrying capacity, showing the similar peak load of 140.0–142.2 kN regardless of prestressing ratio of 50–70%. Moreover, lower prestressing ratio results in longer second and third stages in (Fig. 6) the load-deflection curves, indicating that T-beams will exhibit larger displacements under the same applied load.

5. Conclusion

In this study, flexural performance of 14 prestressed concrete beams was investigated. The research parameters include concrete strength, reinforcement ratio, and cross-section configuration. The performance of GPC was compared with that of PCC according to both Chinese and American design codes. Additionally, the shear lag effect in concrete structures was analyzed. Finally, a parametric analysis was conducted using finite element methods to further explore the performance of GPC beams. The principal conclusions can be summarized as follows:

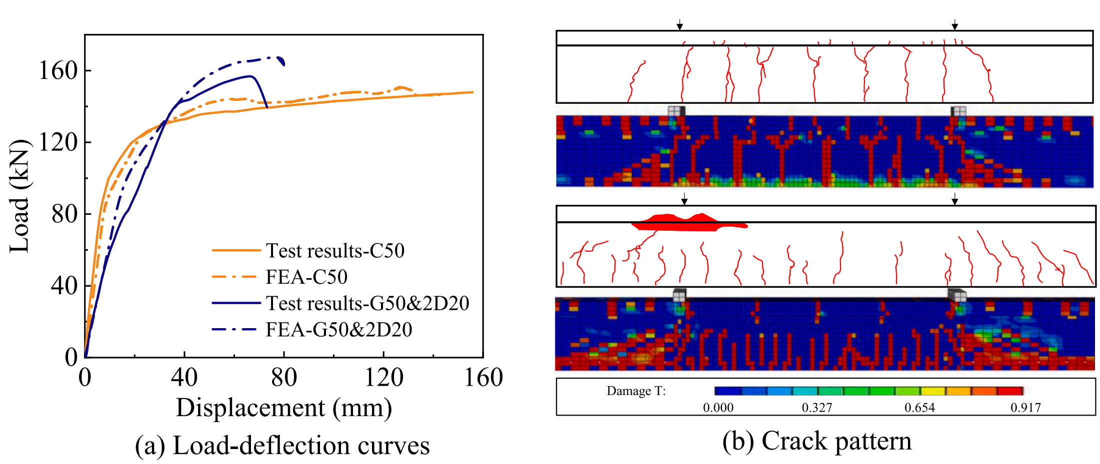

Fig. 16. Comparison between FEA results and test results.

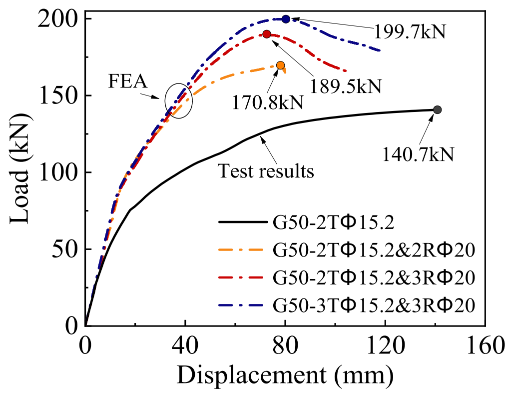

(a) Load-deflection curves according to reinforcement ratio

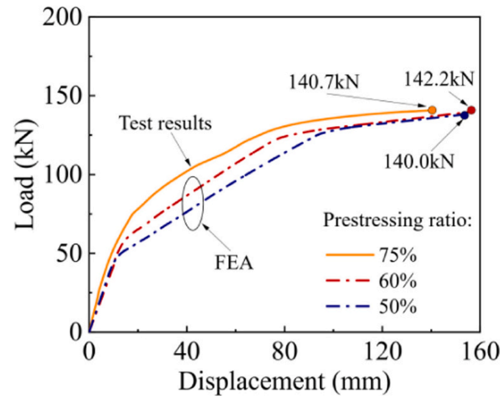

(b) Load-deflection curves according to prestressing ratio

Fig. 17. Comparison of flexural behavior.

1. GPC beams exhibit lower flexural stiffness compared to the corresponding PCC beams. primarily due to the inherently lower elastic modulus and cracking moment of geopolymer concrete. Flexural stiffness increases noticeably with higher reinforcement ratios and concrete strength.
2. The cracking moment of GPC beams is lower than that of PCC beams. The reinforcement ratio and cross-sectional dimensions have little effect on the cracking moment of the beam. The prestressing ratio can improve the crack resistance of the beams.
3. The similarity in the ultimate load capacity between GPC beams and PCC beams arises from the fact that both systems share the same fundamental flexural resistance mechanism, relying on concrete in compression and reinforcement in tension.
4. The pattern of cracks in GPC beams resemble those of PCC beams, with cracks primarily occurring along the stirrup locations. As the reinforcement ratio increases, the number of bending cracks increases, and the average distance between cracks decreases.
5. The applicability of the current design methods in the Chinese code (GB 50010–2010) and the American code (ACI 318–25) for geopolymer concrete was evaluated. Both codes exhibit only minor differences in predicting the short-term stiffness and cracking moment. Moreover, ACI 318–25 provides a more accurate estimation of stress of tendon and is therefore more suitable for estimating the ultimate flexural moment of GPC beams.
6. DIC−3D technology was applied to measure the shear lag effect at the top flange of prestressed beams, enabling full-field strain distribution analysis. The test results show that the effective flange width of the GPC T-beam is overestimated by GB 50010–2010 and ACI 318–25.

CRediT authorship contribution statement

Guoxu Zhao: Writing – original draft, Visualization, Validation, Software, Methodology, Investigation, Formal analysis, Data curation. **Gao Ma:** Writing – review & editing, Supervision, Methodology, Investigation, Funding acquisition, Conceptualization, Validation. **Hyeon-Jong Hwang:** Writing – review & editing, Investigation, Funding acquisition. **Caijun Shi:** review & editing, Funding acquisition, Conceptualization. **Yunxing Du:** Writing – review & editing , Conceptualization.

Declaration of Competing Interest

The authors declare that they have no known competing financial interests or personal relationship that could have appeared to influence the work reported in this paper.

Acknowledgements

The present research was supported by the National Natural Science Foundation of China (No. 51638008), the Huxiang Youth Talent Support Program of Hunan Province, (Grant No. 2021 RC3041), and the National Research Foundation of Korea (NRF) grant funded by the Korea government (MSIT) (No. RS−2024–00333882).

Data availability

Data will be made available on request.

References

[1] Shi C, Jiménez AF, Palomo A. New cements for the 21st century: The pursuit of an alternative to Portland cement. Cem Concr Res 2011;41:750–63.
[2] Duxson P, Provis JL, Lukey GC, van Deventer JSJ. The role of inorganic polymer technology in the development of 'green concrete. Cem Concr Res 2007;37:1590–7.
[3] Peng C, Mao Y, Li S, Xing Y, Du Y, Shi C. Research progress on the structural performance of reinforced geopolymer concrete columns. J Build Eng 2025;112:113805.
[4] Maranan GB, Manalo AC, Benmokrane B, Karunasena W, Mendis P. Evaluation of the flexural strength and serviceability of geopolymer concrete beams reinforced with glass-fibre-reinforced polymer (GFRP) bars. Eng Struct 2015;101:529–41.
[5] Rangan B. Studies on low-calcium fly ash-based geopolymer concrete. Indian Concr J 2008;3:9–17.
[6] Venkatachalam S, Vishnuvardhan K, Amarapathi GD, Mahesh SR, Deepasri M. Experimental and finite element modelling of reinforced geopolymer concrete beam. Mater Today Proc 2021;45:6500–6.
[7] Monfardini L, Minelli F. Experimental Study on Full-Scale Beams Made by Reinforced Alkali Activated Concrete Undergoing Flexure. Materials 2016;9.
[8] Yost JR, Radlińska A, Ernst S, Salera M, Martignetti NJ. Structural behavior of alkali activated fly ash concrete. Part 2: structural testing and experimental findings. Mater Struct 2013;46:449–62.
[9] Prinsse S, Hordijk DA, Ye G, Lagendijk P, Luković M. Time-dependent material properties and reinforced beams behavior of two alkali-activated types of concrete 2020;21:642–58.
[10] Lee K-M, Choi S, Choo JF, Choi Y-C, Yoo S-W. Flexural and Shear Behaviors of Reinforced Alkali-Activated Slag Concrete Beams. Adv Mater Sci Eng 2017;2017:5294290.
[11] Prachasaree W, Limkatanyu S, Hawa A, Sukontasukkul P, Chindaprasirt P. Manuscript title: Development of strength prediction models for fly ash based geopolymer concrete. J Build Eng 2020;32:101704.
[12] Building code requirements for structural concrete: (ACI 318-25).: Committee ACI.
[13] Australia Standards Concrete Structures (AS3600). Sydney: Committee SA. Standards Australia Committee.
[14] Design of Concrete Structures.: Association CS.
[15] Practical Design of Structural Concrete: CIB-FIP Model Code.: International Council for Research and Innovation in Building and Construction IFfSC. International Council for Research and Innovation in Building and Construction, International Federation for Structural Concrete.
[16] Alex AG, Gebrehiwet T, Kemal Z, Subramanian RB. Structural Performance of Low-Calcium Fly Ash Geo-polymer Reinforced Concrete Beam. Iran J Sci Technol Trans Civil Eng 2022;46:3643–54.

[17] Ahmed HQ, Jaf DK, Yaseen SA. Flexural strength and failure of geopolymer concrete beams reinforced with carbon fibre-reinforced polymer bars. Constr Build Mater 2020;231:117185.

[18] Guide fo r the Design and Construction ofConcrete Reinforced with FRP Bars (ACI 440.1R-15) Farmington Hills: Institute AC.

[19] Kobayashi K, Inoue S, Yamasaki T, Nakano K-i. Alkali aggregate reaction in prestressed concrete beams. Int J Cem Compos Lightweight Concr 1988;10:233–40.

[20] Sonal T, Urmil D, Darshan B. Behaviour of ambient cured prestressed and non-prestressed geopolymer concrete beams. Case Stud Constr Mater 2022;16:e00798.

[21] Grant P Magnuson MUC, Benjamin Z Dymond. Design and performance of precast, prestressed concrete beams made with fly-ash-based alkali-activated concrete. PCI J 2025;70:35–51.

[22] Magnuson GP. Precast, Prestressed Concrete Made with Fly Ash-Based Alkali-Activated Cement: Mixture Design and Procedure. Mechanical, and Structural Performance., 2021. University of Minnesota; 2021.

[23] Building code requirements for structural concrete: (ACI 318–19).: Committee ACI.

[24] Neupane K, Hadigheh SA. Sodium hydroxide-free geopolymer binder for prestressed concrete applications. Constr Build Mater 2021;293:123397.

[25] Muthuramalingam S, R T, Thiyagarajan SV, Padmapriya V. Behav Anal Fly Ash Based Prestress Geopolymer Concr Electr Poles 2016:2247–51.

[26] Kastiukas G, Ruan S, Liang S, Zhou X. Development of precast geopolymer concrete via oven and microwave radiation curing with an environmental assessment. J Clean Prod 2020;255:120290.

[27] Qian Z, Zhang S, Ye G, Matthys S, Luković M. Time-dependent flexural behaviour of prestressed alkali-activated concrete (AAC) girder with cast-in-situ AAC topping. Constr Build Mater 2025;484:141615.

[28] Code for Design Concrete Structures (GB50010-2010). Beijing, Chinses: Research CAoB.

[29] The American Association of State Highway and Transportation Officials (AASHTO). Washington DC: Officials AAoSHaT. American Association of State Highway and Transportation Officials.

[30] Yang K-H, Mun J-H, Lee J-S. Flexural tests on pre-tensioned lightweight concrete beams. Proceedings of the Institution of Civil Engineers - Structures and Buildings, 167; 2014. p. 203–16.

[31] Abhishek Yadav AY, Vikas Srivastava VS, Ashok Kumar Tiwari AKT, Parah Salsabeel Jalal PSJ. Evaluating Mechanical Strength of Geopolymer Concrete: Influence of Alkali Activator Ratios and Material Proportions. Int J Adv Eng Manag 2025;7:282–93.

[32] Hu X, Shi Z, Shi C, Wu Z, Tong B, Ou Z, et al. Drying shrinkage and cracking resistance of concrete made with ternary cementitious components. Constr Build Mater 2017;149:406–15.

[33] Fang G, Ho WK, Tu W, Zhang M. Workability and mechanical properties of alkali-activated fly ash-slag concrete cured at ambient temperature. Constr Build Mater 2018;172:476–87.

[34] Dwibedy S, Panigrahi SK. Factors affecting the structural performance of geopolymer concrete beam composites. Constr Build Mater 2023;409:134129.

[35] Li T, Ma G, Hwang H-J, Martí-Vargas JR, Shi C. Evaluation of transfer length in pretensioned geopolymer concrete beams. Eng Struct 2025;339:120605.

[36] Standard for test methods of concrete physical and mechanical properties(GB/T 50081–2019). Beijing: China MoCotPsRo. Ministry of Construction of the People's Republic of China.

[37] Standard for test methods of concrete structures (GB/T 50152–2012). Beijing: China. MoHaU-RDotPsRo. Ministry of Housing and Urban-Rural Development of the People's Republic of China.

[38] Gao X, Yu QL, Brouwers HJH. Assessing the porosity and shrinkage of alkali activated slag-fly ash composites designed applying a packing model. Constr Build Mater 2016;119:175–84.

[39] Hu X, Shi C, Zhang Z, Hu Z. Autogenous and drying shrinkage of alkali-activated slag mortars. J Am Ceram Soc 2019;102:4963–75.

[40] Ehsani MR, Saadatmanesh H, Tao S. Bond Behavior of Deformed GFRP Rebars. J Compos Mater 1997;31:1413–30.

[41] Faza SS, GangaRao HV. Bending and bond behavior of concrete beams reinforced with plastic rebars. Transp Res Rec 1991.

[42] Morcous George, Hanna Kromel, Tadros MK. Bottom Flange Reinf NU I-Girders 2010.

[43] Zhao G, Ma G, Hwang H-J, Shi C, Du Y. Shear behavior and strength prediction model of prestressed slag-based geopolymer concrete beams. Eng Struct 2026;362:122874.

[44] Loov RE. A General Equation for the Steel Stress for Bonded Prestressed Concrete Members. PCI J 1988;33.

[45] Shibayama A, Nishiyama M. Flexural strength and load–deformation relationship of fly-ash-based geopolymer concrete beams. Jpn ARCHITECTURAL Rev 2023;6:e12331.

[46] Hassan A, Arif M, Shariq M, Alomayri T. Experimental test and finite element modelling prediction on geopolymer concrete beams subject to flexural loading. Innov Infrastruct Solut 2022;7:13.

[47] Dai L, Tao Y, Yuan P, Wang L. 3D meso-scale modeling of bond behavior between helical strand and concrete. Eng Struct 2024;309:118041.

[48] Wang L, Zhang X, Zhang J, Yi J, Liu Y. Simplified Model for Corrosion-Induced Bond Degradation between Steel Strand and Concrete. J Mater Civil Eng 2017;29:04016257.